crystals

MDPI

Article

Non-Calcined Metal Tartrate Pore Formers for Lowering Sintering Temperature of Solid Oxide Fuel Cells

Mehdi Choolaei [1], Mohsen Fallah Vostakola [2] and Bahman Amini Horri [1,*]

[1] School of Chemistry and Chemical Engineering, University of Surrey, Guildford GU2 7XH, UK; mehdi.choolaei@cerespower.com
[2] School of Metallurgy and Materials Engineering, Iran University of Science and Technology, Tehran 16846-13114, Iran; mfallah69@metaleng.iust.ac.ir
* Correspondence: b.aminihorri@surrey.ac.uk

Abstract

This paper investigates the application of non-calcined metal tartrate as a novel alternative pore former to prepare functional ceramic composites to fabricate solid oxide fuel cells (SOFCs). Compared to carbonaceous pore formers, non-calcined pore formers offer high compatibility with various ceramic composites, providing better control over porosity and pore size distribution, which allows for enhanced gas diffusion, reactant transport and gaseous product release within the fuel cells' functional layers. In this work, nanocrystalline gadolinium-doped ceria (GDC) and Ni-Gd-Ce-tartrate anode powders were prepared using a single-step co-precipitation synthesis method, based on the carboxylate route, utilising ammonium tartrate as a low-cost, environmentally friendly precipitant. The non-calcined Ni-Gd-Ce-tartrate was used to fabricate dense GDC electrolyte pellets (5–20 μm thick) integrated with a thin film of Ni-GDC anode with controlled porosity at 1300 °C. The dilatometry analysis showed the shrinkage anisotropy factor for the anode substrates prepared using 20 wt. The percentages of Ni-Gd-Ce-tartrate were 30 wt.% and 40 wt.%, with values of 0.98 and 1.01, respectively, showing a significant improvement in microstructural properties and pore size compared to those fabricated using a carbonaceous pore former. The results showed that the non-calcined pore formers can also lower the sintering temperature for GDC to below 1300 °C, saving energy and reducing thermal stresses on the materials. They can also help maintain optimal material properties during sintering, minimising the risk of unwanted chemical reactions or contamination. This flexibility enables the versatile designing and manufacturing of ceramic fuel cells with tailored compositions at a lower cost for large-scale applications.

Keywords: pore former; shrinkage; sintering; ceramic composites; microstructure; fabrication; solid oxide fuel cell (SOFC)

check for updates

Academic Editor: Fan Yang

Received: 30 May 2025
Revised: 3 July 2025
Accepted: 9 July 2025
Published: 10 July 2025

Citation: Choolaei, M.; Vostakola, M.F.; Amini Horri, B. Non-Calcined Metal Tartrate Pore Formers for Lowering Sintering Temperature of Solid Oxide Fuel Cells. *Crystals* **2025**, *15*, 636. https://doi.org/10.3390/cryst15070636

Copyright: © 2025 by the authors. Licensee MDPI, Basel, Switzerland. This article is an open access article distributed under the terms and conditions of the Creative Commons Attribution (CC BY) license (https://creativecommons.org/licenses/by/4.0/).

1. Introduction

Solid oxide fuel cells (SOFCs) have the potential to contribute significantly to the development of sustainable and efficient energy systems. These electrochemical devices convert chemical energy directly into electrical energy, offering high efficiency and low emissions. SOFCs have the potential to revolutionise the energy landscape by providing clean and reliable power generation for a range of applications, including stationary power plants, transportation and portable electronics [1,2]. With their ability to operate on various fuels, such as hydrogen, natural gas and biogas, SOFCs offer versatility and

compatibility with existing infrastructure. Furthermore, their long lifespan, fuel flexibility and potential for combined heat and power generation make them a promising technology for a sustainable energy future [3–5].

The sintering process is a critical step in the fabrication of SOFCs, where ceramic materials are heated to high temperatures to achieve densification [6]. However, conventional high-temperature sintering techniques often present challenges, including thermal stresses, grain growth and reduced material properties. By reducing the sintering temperature, energy consumption and the associated costs can be minimised while also allowing for improved material properties, scalability, a wider choice of materials and compatibility with a broader range of materials [7,8]. A high degree of shrinkage in the anode substrate can be advantageous for the densification of the electrolyte film at lower temperatures [9]. During the co-sintering process of an electrolyte–anode bilayer, the electrolyte and the anode substrate shrink together. In this case, the anode substrate's sintering behaviour plays a crucial role in driving the densification process of the supported electrolyte film. The sinterability of the anodic substrate directly influences the driving force. A higher sinterability of the anode support results in a stronger driving force. Therefore, it is generally preferable to use anode materials with high sinterability in the fabrication process of anode-supported SOFCs [9,10]. In an anode-supported configuration, if the shrinkage mismatch with respect to temperature is beyond a certain limit, the stresses imposed by the support (here, the anode) can serve as an essential source of process flaws, resulting in significant performance losses upon operation. The sintering behaviour of the support is commonly controlled by the microstructural characteristics and the packing structures of both layers [11,12]. A new approach, called anode-assisted sintering, is proposed to lower the sintering temperature and enhance the densification of the anode material. This method utilises the high rate of sinterability of some of the cell layers to improve the sintering of the rest of the layers by implementing compressive forces during the sintering process. This method can tackle the challenges imposed by the traditional high-temperature sintering methods, which can lead to thermal stresses, grain growth and reduced material properties [13–15]. Implementing the suggested internal-anode-assisted densification process can provide a scalable and cost-effective solution to address the existing challenges associated with low-temperature fabrication processes. This improvement is crucial for enhancing the commercial viability of low-temperature SOFCs (LT-SOFCs) in the future [13,16].

Pore formers play a significant role in the sintering process of SOFCs. A pore former is a material added to the ceramic powder mixture to create pores or voids in the green body, which are then retained or removed during sintering [17,18]. Pore formation usually occurs due to the incomplete densification process (known as intrinsic porosity) or by using pore formers, such as graphite, polymers, etc. These pore formers burn out during sintering, leaving behind pores [19]. Pore formers introduce porosity through their decomposition and volatilisation during the heating stage of sintering. The decomposition temperature range of the pore formers ensures that pore formation occurs prior to extensive densification, which takes place at higher temperatures. This allows pores to be distributed throughout the matrix without significantly impeding particle rearrangement and grain growth [17,20]. Once formed, pores must remain stable under high-temperature sintering and during long-term operation. A rigid ceramic framework (e.g., YSZ, GDC or NiO) helps stabilise the pore network by acting as a mechanical scaffold, pinning grain boundaries to inhibit excessive growth and preventing pore shrinkage through Zener pinning effects. At high temperatures, while some pore coarsening occurs due to surface diffusion and pore merging, the porosity levels remain largely unchanged, particularly in samples with moderate pore former loading. This suggests that the remaining matrix is able to maintain structural integrity and resist excessive pore collapse [21–23]. The formation and stability of pores in SOFC

anodes involve complex interactions between pore-forming agents, sintering conditions and microstructural evolution. While pore-forming agents like green pore formers (Green-PF) effectively generate porosity during low-temperature burnout, maintaining this porosity at high operating temperatures requires a stable ceramic framework and careful control of sintering parameters. Understanding these mechanisms allows for better design of durable and efficient SOFC electrodes. Compared to the in situ precipitate pore formers, green pore formers shine in eco-conscious, scalable manufacturing with predictable microstructural outcomes. In contrast, in situ precipitate pore formers offer advanced pore architecture but demand tighter control and may introduce variability in industrial settings [24,25].

Pore formers can lower the sintering temperature of SOFCs by creating the pathways for gas diffusion and reducing the density of the green body. This allows for densification to occur at lower temperatures, facilitating the removal of trapped gases and volatiles during sintering and minimising grain growth and thermal stresses [26,27]. This can result in higher material density and improved mechanical strength of the fuel cell. Pore formers create voids or pores within the green body, which can act as channels for gas diffusion, reactant transport and product release within the fuel cell [28,29]. Properly controlled porosity can optimise gas permeability, fuel cell performance and electrode–electrolyte interactions. They can also help maintain the thermal expansion coefficient of the ceramic material, which is crucial for preventing thermal stresses and cracking during the sintering process and fuel cell operation [30,31]. It is important to note that the type, size, distribution and amount of the pore former used should be carefully optimised to achieve the desired porosity, microstructure and performance of the SOFC [18,32]. Different types of pore formers have been used in the fabrication of SOFC electrodes, including carbon-based materials (such as graphite or carbon black) [33], starch-based materials (derived from potato, corn, etc.) [22], polymer-based compounds (such as PEG, PVA, PMMA, etc.) [26,34], sacrificial materials (such as sugar, ammonium bicarbonates and citric acid) [35] and template-based compounds (such as polystyrene beads or cellulose) [36]. The choice of the pore former depends on various factors, including the desired porosity, material compatibility, sintering conditions and specific requirements of the SOFC application. Generally, carbon-based compounds are the most common materials used as pore formers in SOFCs [33]. The selection of suitable pore formers and their incorporation into the ceramic powder mixture is a critical aspect of SOFC fabrication and can significantly impact the sintering behaviour and properties of the final fuel cell. Optimisation of the type, size, distribution and amount of the pore former is crucial to achieve the desired microstructure and performance of the fuel cell [26,27]. A comparison between different pore formers is shown in Table 1 [37].

Table 1. Comparative analysis of some of the most widely used pore formers.

Pore Former Type	Advantages	Limitations	Thermal Stability
Carbon-based (e.g., graphite, carbon black)	Biodegradable and eco-friendly, low residue after burnout, good pore uniformity	Limited commercial availability, less studied in SOFCs	Moderate to high (depends on formulation)
Polymer-based (PMMA, PVP, . . .)	Precise control over pore size, widely available, compatible with tape casting	May leave residue if not fully decomposed, requires a careful burnout profile	High (PMMA decomposes cleanly at ~400–500 °C)
Starch-based (e.g., rice, potato starch)	Natural and low-cost, produces interconnected pores, easy to handle	Variable decomposition behaviour, may affect slurry rheology	Moderate (decomposes at ~300–400 °C)
Other bio-based (e.g., cellulose, chitosan)	Renewable and sustainable, can enhance mechanical strength, tunable porosity	Less consistent pore morphology, may require additives for uniformity	Moderate to high depending on type
Green-PF	Eco-friendly and biodegradable, low residue after burnout, good pore uniformity	Limited commercial availability, less studied in SOFCs compared to others	Moderate to high (depends on formulation)

Generally, Green-PF offers better dimensional control and microstructural uniformity, making it ideal for multilayer co-sintering and thin electrolyte fabrication. On the other

hand, C-PF is widely used and cost-effective but may introduce variability in shrinkage and pore connectivity, affecting mechanical and electrochemical performance. Table 2 briefly compares the two types of pore formers [17,28,37].

Table 2. Comparison of some microstructural parameters of C-PF (graphite + carbon) and green pore formers.

Property	Green-PF	C-PF
Shrinkage mismatch	Low, promotes isotropic shrinkage	Higher mismatch, may cause anisotropic distortion
Porosity	Uniform and tunable, typically 45–55%	Often broader distribution, porosity 40–60%
Pore morphology	Rounded and interconnected, low tortuosity	Irregular and elongated, higher tortuosity
Electrolyte density	Higher post-sintering density due to better packing	Slightly lower due to residual carbon burnout voids

Non-calcined pore formers offer exciting advantages over the other types, including lower sintering temperature, enhanced porosity control, reduced carbon footprint, higher cost effectiveness, a wider range of material compatibility, minimised risk of unwanted chemical reactions or contaminants, etc. Since the anode thickness for all the anode-supported cells fabricated in this study exceeded 300 µm, a pore-forming agent was added to the anode formula to enhance mass transfer processes through the anode layer. This study investigated the effect of two different pore formers on the final microstructure and sintering behaviour of the Ni-based anode supports using a scalable, consistent and cost-effective fabrication process based on internal-anode-assisted densification of the GDC electrolyte. In this regard, the performance of a graphite and nano-sized carbon mixture (C-PF) was compared with a novel method of using the Ni-Gd-Ce-tartrate precipitate of each anode as its pore former (Green-PF). The Green-PF was used as a reliable and novel pore former in the fabrication of anode-supported SOFCs, which is based on the same elements and composition of the powder constituting the anode substrate material (Ni, Ce and Gd) and transforms to their corresponding metal oxides during burnout and sintering. The main advantage of this pore former is that after its removal, its residue's sintering and surface characteristics are identical to those of the anode oxide powders employed for the anode substrate.

2. Materials and Methods

2.1. Raw Materials

Cerium (III) nitrate ($Ce(NO_3)_3{\cdot}6H_2O$, Sigma-Aldrich), gadolinium (III) nitrate ($Gd(NO_3)_3{\cdot}6H_2O$, Sigma-Aldrich) and dibasic ammonium tartrate ($(NH_4)_2C_4H_4O_6$, Sigma-Aldrich, Gillingham, Dorset, UK) were used as the starting materials without any further purifications. An 85:15 wt.% mixture of graphite (TB-17, MTI), nano-sized carbon powder (<100 nm nanopowder, Sigma-Aldrich), polyvinylpyrrolidone (PVP, average Mw~10,000, Sigma-Aldrich) and ethyl cellulose (viscosity 10 cP, Sigma-Aldrich) were used as a pore former, dispersant and binder, respectively. α-terpineol ($C_{10}H_{18}O$, Supelco, analytical grade) and ethylene glycol ($C_2H_6O_2$, Sigma-Aldrich, anhydrous, 99.8%) were used as solvents in formulating the electrolyte and electrode inks/pastes. All powder preparation methods, such as ball milling, were applied in an ethanol medium using absolute ethanol (CH_3CH_2OH, Sigma-Aldrich, 99.8%).

2.2. Synthesis Method

The synthesis of GDC samples was performed using a recently developed single-step co-precipitation technique described in our previous work [15]. In this regard, the weight fraction of C-PF in the anode formula was calculated based on the weight of C-PF relative to the total amount of anode cermet and C-PF (anode cermet + C-PF). Two different anode samples containing 5 wt.% and 10 wt.% of C-PF were prepared for each type of anode material, respectively, referred to as A5% C-PF and A10% C-PF. On the other hand, Green-PFs and anode cermets were mixed based on volume fractions, where the volume fraction of Green-PF was calculated based on the volume of Green-PF relative to the total volume of anode cermet and Green-PF. Three different anode samples containing 20 vol.% (A20%Green-PF), 30 vol.% (A30%Green-PF) and 40 vol.% (A40%Green-PF) of Green-PF were prepared for each type of anode material. The skeletal density of the powders was used for such calculations, measured by gas pycnometry. To mix the anode cermet and the pore former, wet ball milling in ethanol (at 70 rpm using Capco mdl. 12VS Ball Mill Tumbler and 0.3 cm spherical YSZ balls) was used for 10 min, following the guideline presented in Figure 1. The recovered mixture was dried under vacuum at 50 °C for 2 h and hand ground for 10 min. Polyvinyl alcohol (PVA, average Mw ~130,000, 99+% hydrolysed, Sigma-Aldrich) was added to the anode formula as a suitable binder. An amount of 2 wt.% of PVA was added to all formulated anode powders, where the weight fraction of PVA was calculated based on the weight of PVA relative to the total weight of anode cermet, pore former and PVA. In this process, PVA (appropriate for the production of 2 g of anode powder) was first dissolved in 0.5 mL of deionised water under stirring at 50 °C for 1 h in a 15 mL vial. Then, 4 mL of ethanol was slowly added to the stirring solution, where the solution started to become cloudy. After 1 h of stirring, the prepared mixture of anode cermet and pore former (appropriate for the production of 2 g of anode powder) was then slowly added to the solution and left to stir. After 30 min, 4 mL of ethanol was slowly added to the suspension and stirred for 4 h. The suspension was then dried under vacuum at 50 °C overnight. The recovered anode powder was then ground for 10 min using a mortar and pestle.

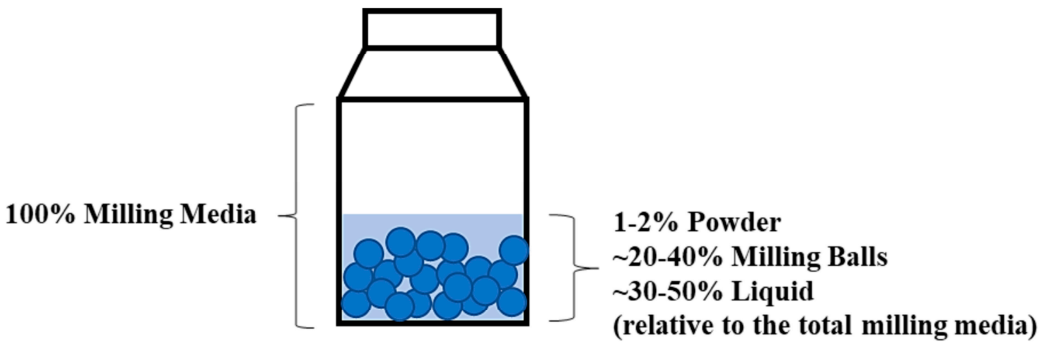


Figure 1. The guideline used for the milling processes in this study.

The prepared anode powder was dry-pressed in a uniaxial dye (⌀ = 20 mm or 15 mm) under ~300 MPa pressure to form button-like pellets. It should be noted that the amount of formulated anode powder used for the fabrication of each supporting anode layer was chosen in such a way that the final amount of anode cermet in all fabricated anode supports remained the same (~0.2 g for 15 mm cells and ~0.4 g for 20 mm cells), regardless of the type or the amount of pore former used. Such restrictions resulted in a slight variation in the thickness of the final supporting anode layers fabricated using different anode formulae (~50 μm). In addition, depending on the cell diameter, ~0.22–0.28 g (for 15 mm cells) and ~0.30–0.40 g (for 20 mm cells) of each anode powder were used to form cells with

thicknesses of 350–450 μm. The anode pellets then underwent pre-sintering in the furnace at 400 °C for 4 h (1.2 °C min^{-1}), followed by an increase to 900 °C for 2 h (1.5 °C min^{-1}). The gradual temperature change during pre-sintering was selected to ensure complete burnout of the pore formers and release of thermal stresses.

For the cell fabrication process, 30 vol% non-calcined metal-tartrate precipitates were used as pore formers, and disk-shaped specimens with a diameter of 15 mm were prepared using uniaxial pressing with ~300 MPa pressure (2 wt.% PVA was added to all samples). The samples were then pre-sintered at 900 °C; then, the electrolyte layer was coated using vacuum spin coating. The anode–electrolyte bilayer was sintered at 1000 °C for 2 h, and then, cathode ink (LSCF-GDC + 10 wt.% C-PF) was used to deposit a narrow layer of cathode with a thickness of about 30 μm on top of the electrolyte layer via spin coating. After drying the cathode layer in the oven, the co-sintering of the completed cells was conducted at 850 °C for 2 h. The fabricated cells were then reduced with hydrogen in a tube furnace at up to 700 °C and a flow rate of 20 mL min^{-1} for 4 h.

2.3. Characterisation

The study utilised a FESEM (JEOL JSM-7100F, JEOL, Tokyo, Japan) with an attached EDX (UltraDry, Thermo Scientific, Waltham, MA, USA) to examine the microstructure of the produced powders and cells. The FESEM was operated with an acceleration voltage between 15 and 20 kV and a probe current of 8–10 nA for optimal elemental characterisation of the samples. The thermal decomposition characteristics of the synthesised precipitates were investigated in this study using a simultaneous differential scanning calorimetry (DSC) and thermal gravimetric analysis (TGA) instrument (SDT Q600, TA Instruments, New Castle, DE, USA). The samples were subjected to heating from 25 °C to 900 °C at a rate of 5 °C min^{-1} under either air or N2 atmosphere.

Dilatometry experiments were conducted using a horizontal dilatometer (DIL 402C, NETZSCH, Selb, Bavaria, Germany) to measure the expansion/shrinkage of the synthesised samples and to determine the optimal sintering temperature for cell fabrication processes. The sintering properties of the samples were analysed in the air over a temperature range of 25–1500 °C, with a heating rate of 4 °C min^{-1}. Depending on the type of analysis, samples were dwelled at temperatures from 1000 to 1500 °C and held for durations of 0–10 h, with 0 dwell time, meaning that the sample cooled down immediately after reaching the programmed sintering temperature. Regarding the dilatometric analysis of the formulated anode powders (containing the pore former), disk-shaped specimens with a thickness of ~2 mm and a diameter of 6.35 mm were also prepared using uniaxial pressing with ~300 MPa pressure. However, the specimens were calcined at 900 °C for 4 h (1.2 °C min^{-1}) prior to the dilatometric analysis to remove the pore former before the analysis.

3. Results and Discussion

Figure 2 illustrates the sintering behaviour of the synthesised NiO-GDC and GDC powders before adding any pore former or making any preparations for the powders. Both samples start to shrink at temperatures around 600 °C with an onset sintering temperature around 500 °C (Figure 2b). However, the synthesised GDC reaches its maximum sintering rate at 850 °C, while the NiO-GDC achieves its highest sintering rate at temperatures as high as 1350 °C. A multistep densification behaviour can be clearly observed for the synthesised GDC sample. In addition to its main sintering peak at 850 °C, two shoulder peaks at 670 °C and 1100 °C can also be detected, each indicating a certain sintering process. During sintering, the contact between GDC particles first results in particle neck formation, followed by densification and grain growth [38]. At the initial sintering stage, low temperatures and mass transport mechanisms mainly occur at the surface and

grain boundaries. Thus, the number of contacts between the particles, which depends significantly on the GDC powder's initial particle and pore size, is of great importance. However, during both the intermediate and final stages of sintering, the densification can be significantly altered by the pinning effects of porosity [39].

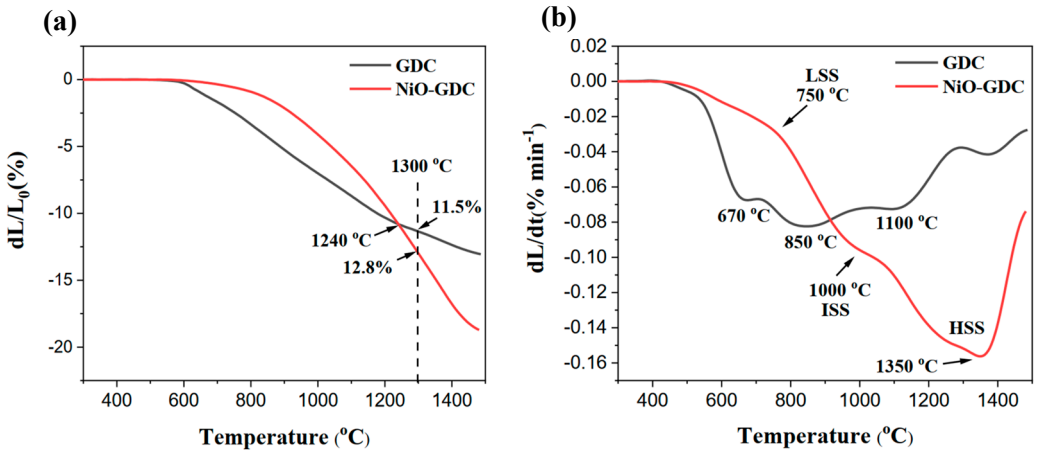


Figure 2. (**a**) Linear sintering shrinkage and (**b**) Rate of the synthesised NiO-GDC and GDC powders.

It can be seen in Figure 2 that the densification behaviour of the synthesised NiO-GDC composite is correlated to its GDC single-phase component. Similar to the GDC powder, the densification of the NiO-GDC composite indicated three main sintering stages (SS) at low (LSS), intermediate (ISS) and high (HSS) temperatures. However, the intermediate (maximum at 1000 °C) and high (maximum at 1350 °C) temperature processes took place at higher temperatures and significantly higher sintering rates than pure GDC.

Two main sintering mechanisms exist during the densification of GDC at intermediate and high temperatures: grain boundary diffusion (grain welding) and grain growth, the latter showing a lower sintering rate [40]. The low maximum sintering rate and corresponding temperature of the synthesised GDC electrolyte could suggest that grain growth is predominant during its densification process. However, in the synthesised NiO-GDC sample, NiO could act as a discontinuous precipitate in the GDC matrix, competing with the GDC grain growth. Such behaviour has been reported in the literature concerning the sintering of alumina through the addition of MgO or NiO [41]. Such prohibition of the GDC grain growth could increase the densification rate at intermediate temperatures by keeping the grain size close to its initial value. In addition, it could promote densification at intermediate temperatures by allowing the grain boundary and porosity (tiny pores) to evolve simultaneously. On the other hand, in a single-phase material like the synthesised GDC electrolyte, the diffusion processes along the grain boundaries are not inhibited, which becomes completely different in the case of the NiO-GDC composite. Since NiO and GDC are only scarcely miscible, the presence of a secondary phase dramatically decreases the chance of same-phase particle contact in the anode composite, retarding the mass diffusion in the anode composite by increasing the mass diffusion distance. Thus, the higher densification activation energy of the NiO-GDC composite shifts the ISS process to higher temperatures compared to the single-phase GDC. Large pores mainly influence the maximum sintering rate at 1350 °C and can be related to their elimination at such elevated temperatures.

One can observe that the GDC sinters more rapidly than the NiO-GDC at temperatures below 900 °C, whereas above 900 °C, the sintering rate of NiO-GDC surpasses that of a single-phase GDC sample, showing a much more significant linear shrinkage at 1500 °C (ca. 18%). In the anode-supported configuration, such high sinteractivity of the synthesised

NiO-GDC sample could be highly beneficial in promoting the densification of the supported GDC electrolyte film during the co-sintering process. It has been illustrated that a high shrinkage of the anode substrate could be beneficial for the electrolyte film densification process at relatively low temperatures [9,42,43]. During the co-sintering process of an electrolyte–anode bilayer, the electrolyte and the anode substrate shrink together. Thus, different from the sintering of a pelletised electrolyte, in addition to the grain growth of the electrolyte material, the sintering promotion of the anodic substrate could act as a decisive driving force for the densification process of the supported electrolyte film. This driving force is directly related to the sinteractivity of the anodic substrate; the higher the sinteractivity of the anode support, the stronger the driving force that is provided. Thus, the use of anode material with high sinteractivity is commonly desirable in the anode-supported SOFC fabrication process [9,10].

A porosity of around 40 vol.% has been reported as appropriate to reach an acceptable strength, gas diffusion and current collection in an operating cell [44]. On the other hand, a good match between the sintering behaviour of the anode substrate and the electrolyte film is of great importance in decreasing the destructive stress between the two layers [32]. The presence of such immoderate stress during sintering could not only result in the delamination and cracking of the electrolyte layer but also constrain the densification of the thin electrolyte film [9,45]. Given the low-temperate fabrication target of 1300 °C in this study and the 11.5% linear shrinkage of the synthesised GDC electrolyte at this temperature (Figure 2a), the shrinkage and porosity of the anode substrate should be controlled to be as close as possible to 11.5% and 40% at the targeted sintering temperature, respectively.

Figure 3 illustrates the linear sintering shrinkage and rate of both A5%C-PF and A10%C-PF anode substrates along with the sintering shrinkage and rate of NiO-GDC and GDC powders, for comparison purposes. Since the evaluated anode substrates were pre-sintered at 900 °C (in air), both illustrated a slight expansion up to 900 °C before indicating a drastic sintering rate. The addition of 10%C-PF to the anode formula was shown to reduce the final shrinkage mismatch between the anode substrate (10.8%) and the GDC electrolyte (11.5%). However, a further match for the shrinkage rate at the ISS was observed by reducing the amount of the C-PF to 5% (Figure 3b). As expected, the porosity of the anode substrate increased with the increase in the amount of C-PF in the anode composition. The porosity of the samples after sintering and reduction with hydrogen at 900 °C was determined to be 37% and 45% for A5%C-PF and A10%C-PF, respectively. Despite their close porosity, the final linear shrinkage of A5%C-PF was shown to be less than half that of A10%C-PF. Such a small variation in porosity but an appreciable increase in linear shrinkage could indicate that the micropores developed at the sites of C-PF are rather unstable. Thus, a considerable amount of the pores disappears during the high-temperature sintering of the substrate, causing a substantial rise in the linear shrinkage and a small variation in porosity. The difference in the shrinkage behaviour of A5%C-PF and A%C-PF at the ISS could be attributed to the higher number of micropores in the A10%C-PF substrate. As mentioned before, such micropores will readily shrink during the ISS, and the combined effect of the shrinkage of a large number of micropores gives rise to the larger linear shrinkage and sintering rate in the A10%C-PF substrate. It should be noted that the high shrinkage mismatch between the A5%C-PF substrate (4.8%) and the GDC electrolyte (11.5%) could result in the cracking and/or delamination of the electrolyte film during the co-firing process. The intense sintering rate observed at temperatures above 1250 °C for both samples could be related to the expulsion of large pores from the substrate matrix.

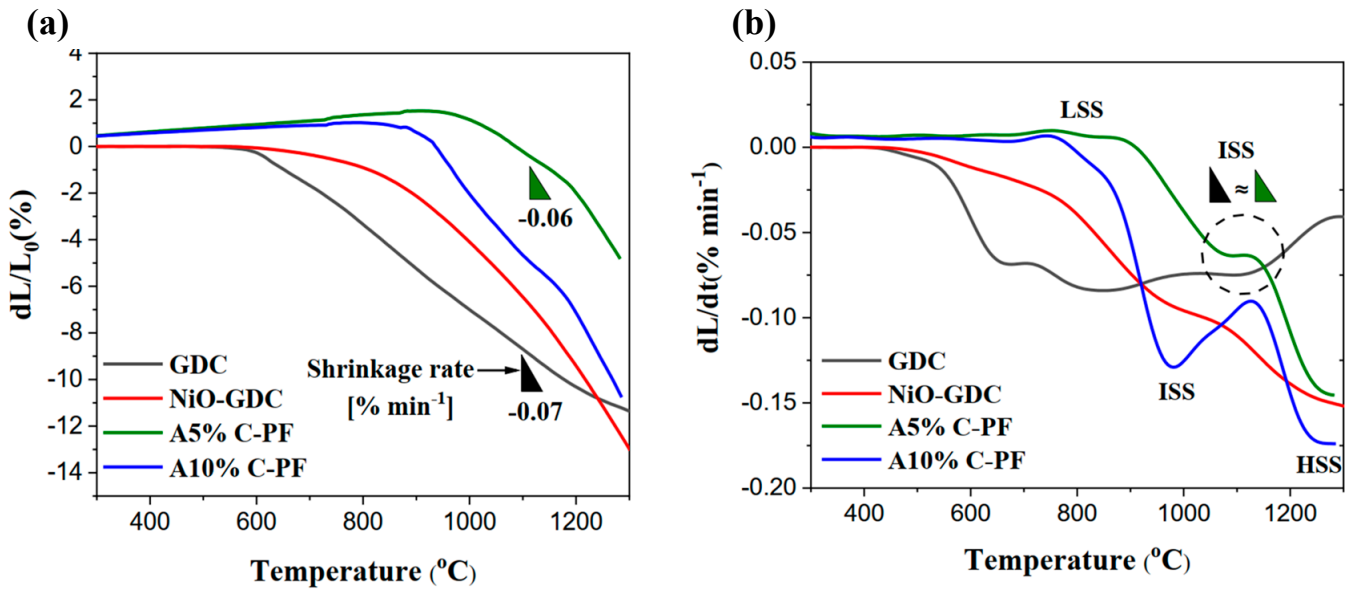


Figure 3. Linear sintering: (**a**) Shrinkage and (**b**) Rate of the A10%C-PF and A5%C-PF substrates along with the synthesised NiO-GDC and GDC powders.

As an important component of SOFCs, the electrolyte layer should demonstrate a high level of densification to successfully separate the fuel gas from the air. Figure 4a–d present the FESEM images of the GDC electrolyte films deposited on A5%C-PF and A10%C-PF anode substrates after co-sintering at 1300 °C. For comparison purposes, the FESEM micrographs of the pelletised GDC electrolyte after densification at 1300 °C are also presented (Figure 4e,f). For both A5%C-PF and A10%C-PF substrates, the GDC membranes were rather porous after co-sintering, suggesting the need for higher sintering temperatures. However, it can be seen in Figure 4e,f that the pelletised GDC electrolyte reaches high densification levels at 1300 °C (over 94% relative density), which itself shows the high sinteractivity of the synthesised GDC electrolyte. Thus, considering the small linear shrinkage mismatch between A10%C-PF substrate and GDC powder, along with the relatively high sintering rate of A10%C-PF at ISS and HSS, one would assume a much higher electrolyte densification for the GDC/A10%C-PF bilayer. However, on the contrary, the co-fired GDC/A5%C-PF bilayer with a significantly larger shrinkage mismatch illustrated a much higher densification for the electrolyte membrane (Figure 4c,d).

The difference observed in the densification of the pelletised GDC electrolyte and the deposited GDC films is linked to the difference in the approaches applied in the preparation of their green parts. The use of vacuum spin coating for the deposition of the electrolyte layer onto the anode substrates could lead to a lower packing density compared to the pelletised GDC electrolyte. The fast drying of the electrolyte ink during spin coating can limit particle rearrangement due to the rapid decrease in the liquid vehicle. Contrarily, the uniaxial press used to pelletise the GDC powder will force the electrolyte particles to rearrange into a high-packing form, facilitating the densification process, especially at low sintering temperatures. However, this does not explain the difference observed in the densification of the GDC films between the two anode substrates, where the substrate with a higher linear sintering shrinkage illustrated lower electrolyte film density. In the anode-supported configuration, the sintering promotion of the anodic substrate could act as a decisive driving force for the densification process of the supported electrolyte film, where the higher the sinteractivity of the anode support, the stronger the driving force that is provided.

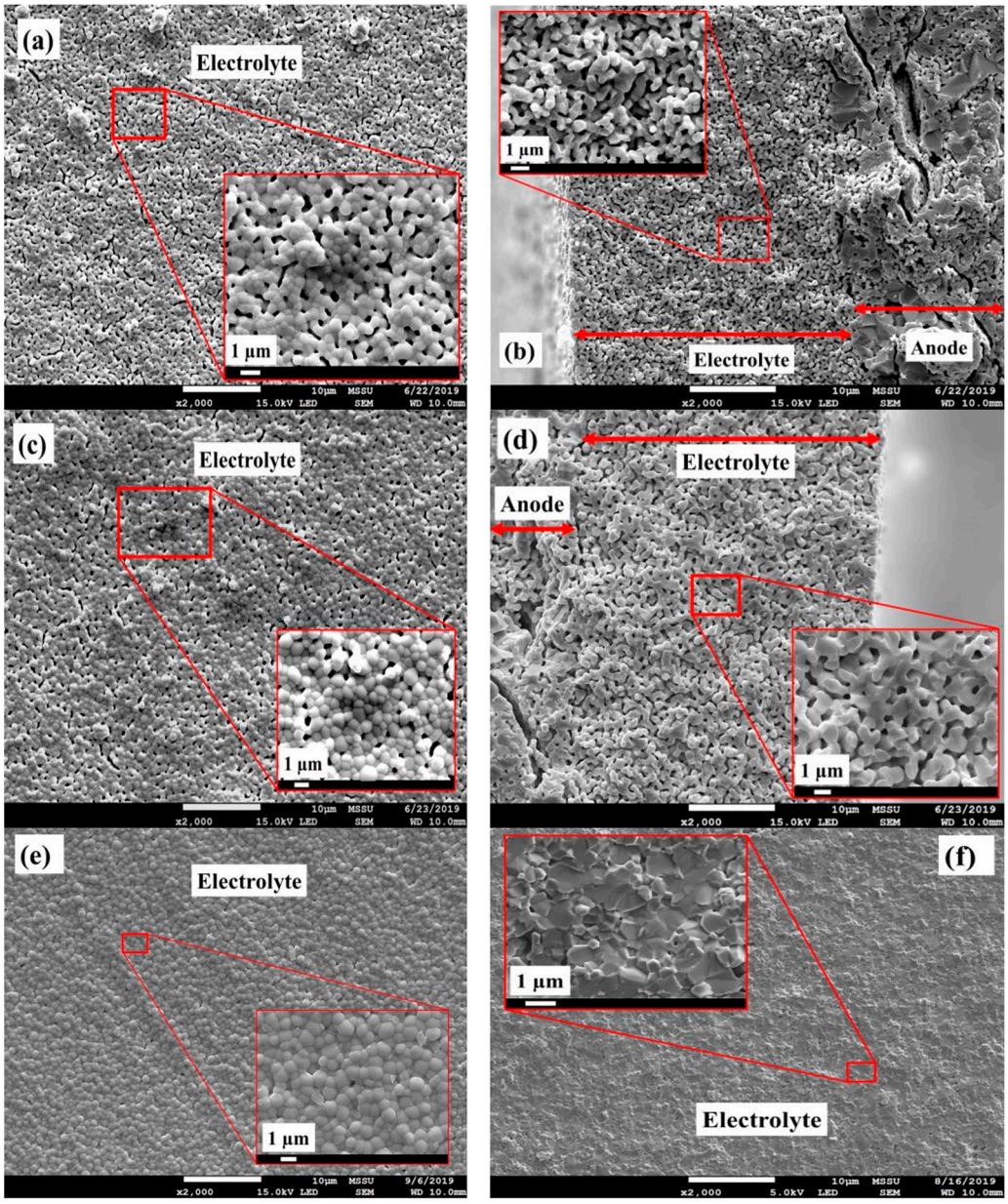


Figure 4. FESEM images of the top view (**a**,**c**) and cross-section (**b**,**d**) of the GDC electrolyte layer on A10%C-PF (**a**,**b**) and A5%C-PF (**c**,**d**) substrates, co-sintered at 1300 °C for 5 h. (**e**,**f**) illustrate the top view and cross-section, respectively, of the pelletised GDC electrolyte sintered at 1300 °C for 5 h.

Although thermodilatometry is a powerful tool to study the sinterability of ceramic material, it can only provide a one-dimensional analysis during sintering, while in some cases, the sintering changes do not take place uniformly over the examined specimen. With the configuration used in this study, the dilatometer can only measure the axial shrinkage, and thus, the radial shrinkage of the analysed samples is unknown. To evaluate the radial shrinkage, an anisotropy factor (K) was required for the analysed specimens. To determine the value of the anisotropy constant for the pelletised GDC electrolyte and the anode substrates, first, the fired density (density after sintering) of the specimens was measured directly using the Archimedes method. Second, based on the linear shrinkage data recorded from the thermodilatometry tests and the measured green density of the specimen, the fired density of the sample was calculated, assuming isotropic shrinkage. Then, the two fired densities were compared and matched by choosing a K value for each specimen. Thus, by defining K as the ratio of total axial to radial shrinkage, it was possible to estimate the

total radial shrinkage based on the axial shrinkage and fired density. In this regard, the shrinkage anisotropy factor for GDC, A5%C-PF and A10%C-PF was estimated to be 0.90, 1.06 and 1.21, respectively.

As can be observed, the synthesised GDC electrolyte illustrates higher shrinkage in the radial direction, whereas an opposite behaviour is observed for the A10%C-PF substrate, where the axial shrinkage is predominant. Thus, upon co-sintering of the GDC/A10%C-PF bilayer, the shrinkage occurs mostly in the direction perpendicular to the anode substrate (axial direction), where the in-plane shrinkage (radial shrinkage) of the thin electrolyte layer is inhibited by the external constraints imposed by the anisotropic shrinkage of the anode substrate. In fact, when the amount of C-PF pore former in the anode substrate was decreased to 5%, a more isotropic sintering behaviour (K = 1.06) was observed for the anode substrate, resulting in a higher densification of the thin GDC electrolyte film (Figure 4a,d). Such a change in the shrinkage behaviour of the anode substrate upon variation in the ratio of the pore former could be related to the morphological development of anisotropic pores through the addition of C-PF.

Figure 5 illustrates the microstructural properties of the fabricated A%C-PF substrates sintered at 1300 °C (after reduction at 900 °C in hydrogen). As shown, the microstructure of the anode substrate seems to have been altered by variation in the C-PF ratio in the anode powder. The substrate obtained with 10% C-PF showed a relatively anisotropic or non-uniform pore structure, while reducing the ratio of C-PF to 5% was indeed effective in decreasing the pore anisotropy in the anode substrate. Such microstructural differences between the two substrates can mainly originate from the geometrical anisotropy of graphite in the C-PF mixture. As reported in the literature, anisotropic particles such as graphite could illustrate different percolation behaviours depending on their volume fraction in the anode composite [44,46]. Due to the relatively high specific surface area and hydrophobic surface characteristics of graphite, its uniform dispersion is very difficult to achieve, especially in an aqueous suspension. Thus, typically, graphite particles are the agglomerates of many aggregates consisting of primary particles a few nanometres in size that are bonded together [47]. This structure makes graphite geometrically anisotropic and extremely porous, in addition to giving it a large surface area. Such characteristics of graphite, which are very different from those of metal oxide particles, prevent the formation of a well-dispersed anode composite during the wet ball milling process of graphite and NiO-GDC powders. Thus, when anode composites containing geometrically anisotropic graphite are uniaxially pressed, it is difficult to prevent mutual interactions between large graphite particles in the anode matrix. In this case, increasing the C-PF ratio gives rise to formation of a higher number of randomly dispersed anisotropic pores with non-uniform size distribution (Figure 5b); thus, the linear shrinkage of the anode substrate tends to be more anisotropic at higher C-PF loadings. However, by decreasing the ratio of C-PF to 5%, more uniform and isotropic pores were observed in the anode structure (Figure 5d), increasing the isotropic sintering characteristic of the anode substrate (K = 1.06).

While C-PF was shown to generate additional porosity in the anode substrate, the low pore stability and the anisotropic shrinkage behaviour of the A%C-PF substrates were shown to constrain the densification of the GDC thin film during the co-firing process. Therefore, a novel approach was applied to not only improve the permeability of the anode substrate but also to greatly minimise the constraining effect of the anode substrate on the densification of the thin electrolyte layer.

The difference between the sintering behaviour (linear shrinkage and rate) of the fabricated A%C-PF and A%Green-PF-based substrates can be seen in Figure 6a,b. All three A%Green-PF substrates illustrated almost the same shrinkage behaviour and were very much similar to that of A5%C-PF. The slight difference in the shrinkage rate of the

A%Green-PF samples at ISS could be attributed to the larger number of micropores in the substrates with a higher Green-PF ratio. Thus, the combined shrinkage of such micropores at ISS resulted in a slightly higher linear shrinkage and sintering rate for the A40% Green-PF substrate. Despite such small differences, the shrinkage rate of all three A%Green-PF substrates at ISS remained close to that of the synthesised GDC powder, with A30%Green-PF showing almost the same shrinkage rate at 1100 °C (Figure 6b).

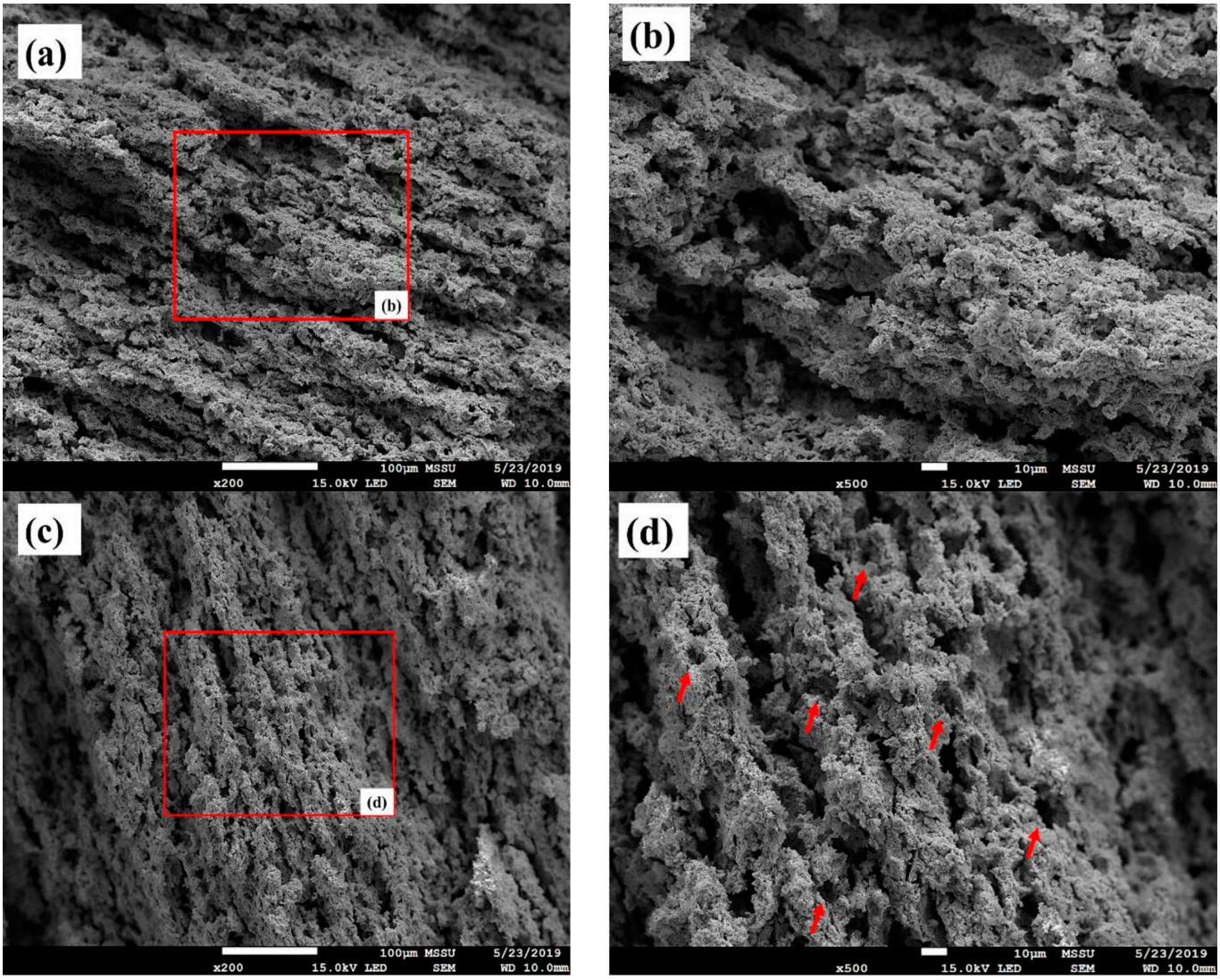


Figure 5. FESEM images of A10%C-PF (**a**,**b**) and A5%C-PF (**c**,**d**) substrates, sintered at 1300 °C followed by reduction at 900 °C under hydrogen. **Note**: The red box shown in (**a**) has been magnified in (**b**), and similarly, the red box in (**c**) is magnified in (**d**). The arrows in (**d**) shows the higher number of randomly dispersed anisotropic pores with non-uniform size distribution, as explained in the last paragraph of page 11.

It is possible to estimate the porosity of a pelletised electrode body, either green or sintered, by comparing the envelope volume of the pellet with the skeletal volume of the same sample measured by gas pycnometry, V_p. It should be noted that due to the limitations of such measurements, the calculated porosity in this work is considered to be an estimation of the porosity of the samples and not the absolute value. Such porosity calculations were used to study the change in the porosity of an anode material when varying the amount or type of the pore former in the anode formula. Thus, defining V_e as the envelope volume of a pellet, the porosity of different pelletised samples was calculated by [48]

$$Porosity\ (open\ pores)\% = \frac{(V_e - V_P)}{V_e} \times 100 \quad (1)$$

Similar to the A%C-PF substrates, the porosity of the A%Green-PF substrates increased when the ratio of Green-PF in the anode composite was increased (Figure 6c). The porosity of the samples after sintering and reduction with hydrogen at 900 °C was found to be 40%, 45% and 52% for A20%Green-PF, A30%Green-PF and A40%Green-PF, respectively. As can be observed in Figure 6a, the sintering shrinkage did not change significantly according to the amount of Green-PF added and remained around 4%, quite the opposite of what was observed for the A%C-PF substrates. Such a negligible change in the shrinkage of the anode substrate, despite the increasing amount of Green-PF added, indicates the fact that the pores developed at the Green-PF sites are rather stable and therefore survive (or do not shrink significantly) throughout the whole sintering process (both the ISS and HSS). Thus, no additional shrinkage due to the addition of Green-PF can be observed.

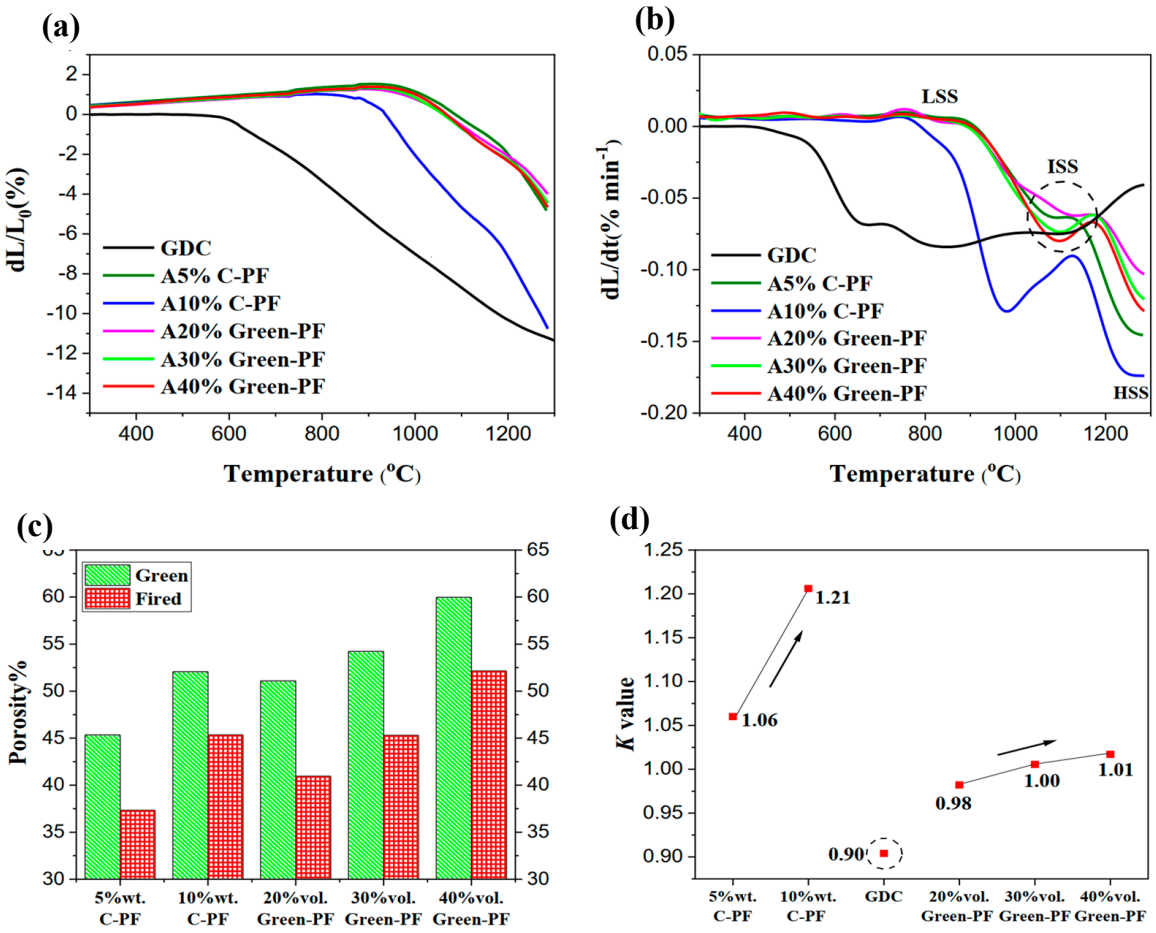


Figure 6. Variation in (**a**) Linear shrinkage and (**b**) Rate, (**c**) Porosity after reduction by hydrogen and (**d**) *K* value of A%C-PF and A%-Green-PF substrates with the amount of pore former added to the anode powder mixture.

The shrinkage anisotropy factor for A20%Green-PF, A30%Green-PF and A40%Green-PF was estimated to be 0.98, 1.00 and 1.01, respectively. Figure 6d provides a comparison between the change in the *K* value estimated for the fabricated A%Green-PF and A%C-PF substrates. As can be observed, A%Green-PF substrates illustrate a much higher isotropic shrinkage than that of substrates fabricated using C-PF as a pore former. Such behaviour could indicate the formation of an isotropic pore structure upon the addition of Green-PF to the anode substrate.

The microstructure of the A20%Green-PF substrate after sintering at 1300 °C is presented in Figure 7a,b. Isotropic spherical pores with a diameter of around 10 μm are uniformly distributed throughout the anode structure and are connected via well-distributed microchannels, forming a pore network channel. Additionally, a porous microstructure was observed surrounding the spherical pores, making the pore network highly beneficial for gas phase transport (Figure 7b). Figure 7c illustrates the cross-section of the GDC/A20%Green-PF bilayer after sintering at 1300 °C (5 h) and reduction at 900 °C under hydrogen flow. The GDC electrolyte layer is about 12 μm thick and shows a high level of densification without major process flaws, where a clear crystalline path between the anode substrate and the top of the electrolyte film can be observed (inset Figure 7c). The electrolyte thickness was shown to be easily controllable by varying the number of coating steps, making it possible to fabricate electrolyte films in the range of 5–20 μm. Despite the presence of a linear shrinkage mismatch between the A20%Green-PF substrate and the electrolyte layer (Figure 6a), the induced stresses did not reach a critical value, and thus, no cracking or delamination of the electrolyte membrane was observed.

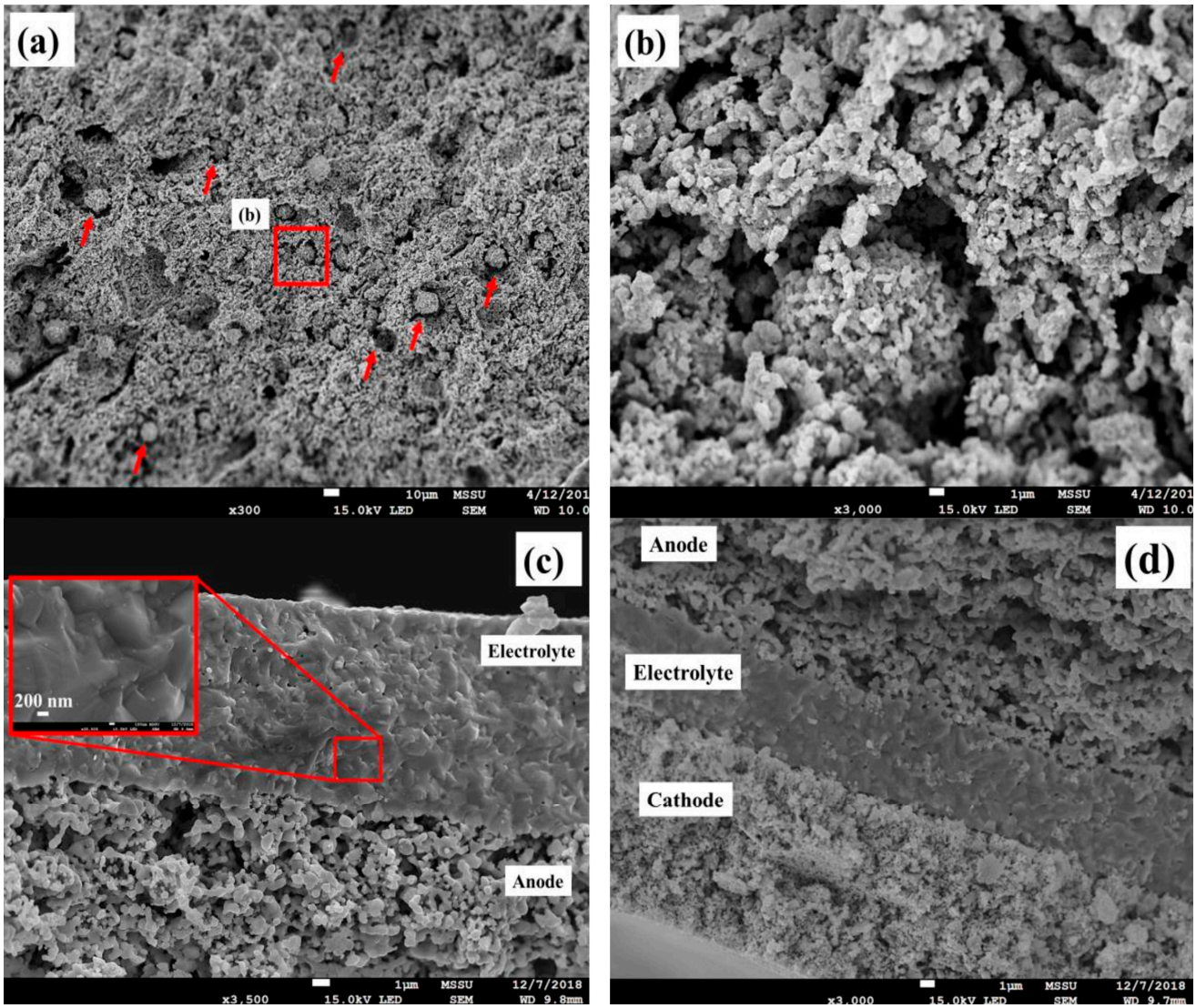


Figure 7. FESEM micrographs of (**a**,**b**) A20%Green-PF after sintering at 1300 °C. (**c**) The cross-section of the GDC/ A20%Green-PF bilayer after co-firing at 1300 °C and reduction under hydrogen flow at 400 °C. (**d**) FESEM cross-section micrograph of the as-prepared NiO-GDC/GDC/LSCF-GDC anode-supported SOFC.

Figure 8 shows the TGA/DSC analysis of the as-prepared Ni-GDC sample. Since the sample already underwent thermal decomposition, it mainly consists of metal oxides; therefore, the weight loss associated with increasing the temperature from 21 to 850 °C is primarily due to dehydration (below 281 °C, equivalent to 1.23 wt.%), followed by a degassing stage (0.63 wt.%). The volumetric change during the phase transformation of Ni-Ce-Gd-tartrate to NiO-GDC can develop micro-sized pores at the Green-PF sites, where the high exothermic character and the sudden release of a large amount of gaseous products during the burnout of Ni-Ce-Gd-tartrate precipitates (Figure 8) result in the formation of a highly porous and stable pore structure in the substrate. Thus, the porosity (ca. 40%), *K* value (0.98), resultant microstructure and sintering behaviour (shrinkage and rate) of the A20%Green-PF substrate were considered to satisfy the requirements for both electrolyte densification during co-firing and the fabrication of high-performance anode-supported SOFCs.

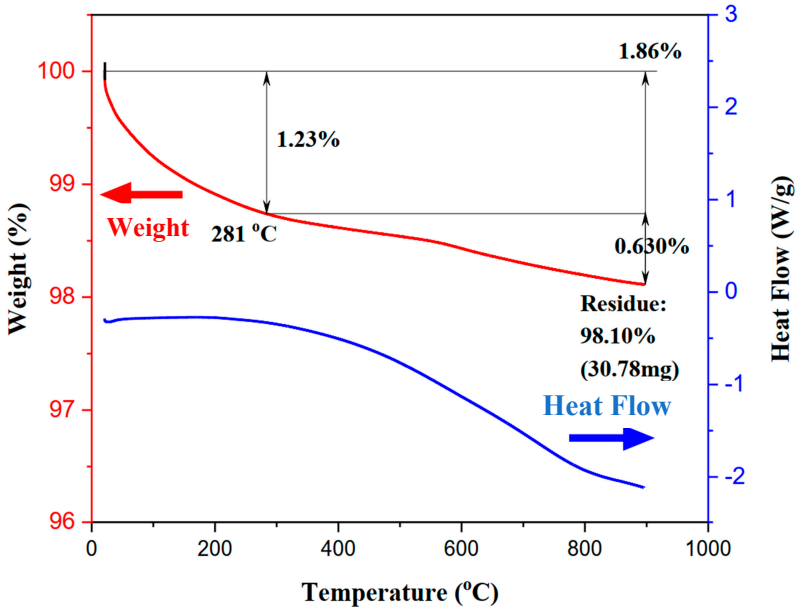


Figure 8. TGA/DSC curves of the thermal decomposition of the as-prepared Ni-GDC sample.

As indicated by the FESEM investigations, the electrolyte layer was shown to cover the surface of the anode substrate in a fairly uniform manner with a very high thickness uniformity, regardless of the presence of surface irregularities (e.g., high surface roughness). Such an achievement is of great deal of importance, since the fabrication of defect-free thin electrolyte films on the surface of anode substrates with high surface roughness is still considered a key challenge, especially at relatively low sintering temperatures and durations [9,49,50]. Many studies have tried to overcome this problem by adopting electrolyte sintering aids and/or improving the roughness of the anode substrate by applying a functional layer with a fine and homogenous pore structure between the electrolyte and anode substrate [9,50]. Although in some cases such approaches are effective, they commonly add more complexity to the fabrication and operating processes surrounding SOFCs. Using LSCF-GDC as the cathode material and spin coating as the cathode deposition process, anode-supported single cells with thin GDC electrolyte films were fabricated. Figure 7d illustrates a cross-section FESEM image of the as-prepared anode-supported single cell. The fabricated cell shows the presence of an open-structured NiO-GDC anode layer, a thin dense GDC electrolyte (6 μm) and a porous LSCF-GDC cathode. The GDC electrolyte layer was shown to adhere very well with both the anode and cathode electrodes, without any sign of cracking or delamination.

4. Conclusions

In conclusion, the importance of lowering the sintering temperature in SOFCs cannot be overstated. The use of non-calcined pore formers in SOFC fabrication has shown promise in reducing energy consumption, lowering production costs and mitigating thermal stresses associated with high sintering temperatures. Additionally, the environmentally friendly nature of non-calcined materials reduces the carbon footprint of the manufacturing process. Furthermore, the ability to control porosity and pore size distribution with non-calcined pore formers offers opportunities for optimising gas diffusion, reactant transport and overall fuel cell efficiency. Dense GDC electrolyte films with a thickness in the range of 5–20 μm were successfully coated on highly porous Ni-GDC anode substrates, using—for the first time—non-calcined Ni-Gd-Ce-tartrate precipitates (Green-PF) as a reliable, cost-effective and novel pore former. The use of Green-PF greatly promoted the densification of the GDC electrolyte layer at 1300 °C (under air) without the need for additional sintering aids and/or anode surface modification processes. Full electrolyte densification was achieved at relatively low sintering temperatures and was based solely on minimising the external constraints imposed by the anisotropic shrinkage of the anode substrate. With regard to the fabrication of anode-supported SOFCs, all synthesised anode and electrolyte powders illustrated a high sinteractivity, promoting the densification of the GDC electrolyte film during the co-sintering process at reduced sintering temperatures. The application of such techniques resulted in the successful fabrication of a structurally dense, physically thin and chemically homogenous GDC electrolyte layer at considerably low sintering temperatures (1100 °C). Overall, it is suggested that future studies should focus on electrochemical performance testing, long-term redox cycling and scale-up implications.

Author Contributions: Writing—Original draft preparation, formal analysis, investigation, data curation, visualisation, M.C.; writing—review and editing, visualisation, M.F.V.; conceptualisation, methodology, validation, funding, writing—review and editing, supervision, B.A.H. All authors have read and agreed to the published version of the manuscript.

Funding: This research received no external funding.

Data Availability Statement: The original contributions presented in the study are included in the article; further inquiries can be directed to the corresponding author.

Conflicts of Interest: The authors declare no conflicts of interest.

References

1. Rauf, S.; Hanif, M.B.; Tayyab, Z.; Veis, M.; Yousaf Shah, M.A.K.; Mushtaq, N.; Medvedev, D.; Tian, Y.; Xia, C.; Motola, M.; et al. Alternative Strategy for Development of Dielectric Calcium Copper Titanate-Based Electrolytes for Low-Temperature Solid Oxide Fuel Cells. *Nano-Micro Lett.* **2025**, *17*, 13. [CrossRef]
2. Choolaei, M.; Jakubczyk, E.; Amini Horri, B. Synthesis and Characterisation of a Ceria-Based Cobalt-Zinc Anode Nanocomposite for Low-Temperature Solid Oxide Fuel Cells (LT-SOFCs). *Electrochim. Acta* **2023**, *445*, 142057. [CrossRef]
3. Han, Z.; Dong, H.; Wang, H.; Yang, Y.; Yu, H.; Yang, Z. Temperature-Dependent Chemical Incompatibility between NiO-YSZ Anode and Alkaline Earth Metal Oxides: Implications for Surface Decoration of SOFC Anode. *J. Alloys Compd.* **2023**, *968*, 172150. [CrossRef]
4. Choolaei, M.; Horri, B.A. Catalytic Aspects of Fuel Cells: Overview and Insights. In *Heterogeneous Catalysis for Energy Applications*; Royal Society of Chemistry: London, UK, 2020; pp. 459–494.
5. Vostakola, M.F.; Ozcan, H.; El-emam, R.S.; Horri, B.A. Recent Advances in High-Temperature Steam Electrolysis with Solid Oxide Electrolysers for Green Hydrogen Production. *Energies* **2023**, *16*, 3327. [CrossRef]
6. Zhang, M.; An, L.; Wang, E.; Wang, H.; Ouyang, M.; Hu, H. Effects of Sintering Parameters on the Low-Temperature Densification of GDC Electrolyte Based on an Orthogonal Experiment. *Catalysts* **2022**, *12*, 831. [CrossRef]
7. Yang, H.; Zhang, Y.; Liu, Z.; Hu, C.; Li, J.; Liao, H.; Shao, M.; Ni, M.; Chen, B.; Shao, Z.; et al. Hydration-Induced Stiffness Enabling Robust Thermal Cycling of High Temperature Fuel Cells Cathode. *Nat. Commun.* **2025**, *16*, 3154. [CrossRef] [PubMed]

8. Fu, P.; Yan, M.; Zeng, M.; Wang, Q. Sintering Process Simulation of a Solid Oxide Fuel Cell Anode and Its Predicted Thermophysical Properties. *Appl. Therm. Eng. J.* **2017**, *125*, 209–219. [CrossRef]
9. Serra, J.M.; Büchler, O.; Meulenberg, W.A.; Buchkremer, H.P. Thin $BaCe_{0.8}Gd_{0.2}O_{3-\delta}$ Protonic Electrolytes on Porous $Ce_{0.8}Gd_{0.2}O_{1.9}$–Ni Substrates. *J. Electrochem. Soc.* **2007**, *154*, 334–340. [CrossRef]
10. Sun, W.; Yan, L.; Shi, Z.; Zhu, Z.; Liu, W. Fabrication and Performance of a Proton-Conducting Solid Oxide Fuel Cell Based on a Thin $BaZr_{0.8}Y_{0.2}O_{3-\delta}$ Electrolyte Membrane. *J. Power Sources* **2010**, *195*, 4727–4730. [CrossRef]
11. Fallah Vostakola, M.; Amini Horri, B. Progress in Material Development for Low-Temperature Solid Oxide Fuel Cells: A Review. *Energies* **2021**, *14*, 1280. [CrossRef]
12. Lee, S.H.; Messing, G.L.; Green, D.J. Warpage Evolution of Screen Printed Multilayer Ceramics during Co-Firing. *Key Eng. Mater.* **2004**, *264–268*, 321–328. [CrossRef]
13. An, H.; Lee, H.W.; Kim, B.K.; Son, J.W.; Yoon, K.J.; Kim, H.; Shin, D.; Ji, H.I.; Lee, J.H. A 5×5 cm^2 Protonic Ceramic Fuel Cell with a Power Density of 1.3 W cm^{-2} at 600 °C. *Nat. Energy* **2018**, *3*, 870–875. [CrossRef]
14. Dai, H.; Kou, H.; Tao, Z.; Liu, K.; Xue, M.; Zhang, Q.; Bi, L. Optimization of Sintering Temperature for SOFCs by a Co-Firing Method. *Ceram. Int.* **2020**, *46*, 6987–6990. [CrossRef]
15. Choolaei, M.; Cai, Q.; Slade, R.C.T.; Amini Horri, B. Nanocrystalline Gadolinium-Doped Ceria (GDC) for SOFCs by an Environmentally-Friendly Single Step Method. *Ceram. Int.* **2018**, *44*, 13286–13292. [CrossRef]
16. Pagliari, M.; Marasi, M.; Montinaro, D.; Vandoni, D.; Martelli, E.; Campanari, S.; Donazzi, A. Electrochemical Performance of LSM-YSZ SOFC Cathodes: Activation, Durability, and Tolerance to CO_2. *J. Power Sources* **2025**, *649*, 237458. [CrossRef]
17. Timurkutluk, C.; Onbilgin, S.; Yildirim, F.; Germen Tutas, G.; Onbilgin, S.; Timurkutluk, B. The Role of Pore Former Type on the Performance of Anode Functional Layer in Microtubular Solid Oxide Fuel Cells. *Int. J. Hydrogen Energy* **2025**, *142*, 886–895. [CrossRef]
18. Laguna-Bercero, M.A.; Hanifi, A.R.; Menand, L.; Sandhu, N.K.; Anderson, N.E.; Etsell, T.H.; Sarkar, P. The Effect of Pore-Former Morphology on the Electrochemical Performance of Solid Oxide Fuel Cells under Combined Fuel Cell and Electrolysis Modes. *Electrochim. Acta* **2018**, *268*, 195–201. [CrossRef]
19. Silveira, C.; Mulinari, J.; Junior, A.D.N.; Ambros, A.; Hotza, D.; Luccio, M. Di Low-Cost Ceramic Membranes Prepared from Kaolin and Quartz via Tape Casting Using Different Pore Formers. *Open Ceram.* **2025**, *22*, 100765. [CrossRef]
20. Jamil, S.; Ahmad, S.H.; Rahman, M.A.; Othman, M.H.D.; Rahman, M.A.; Jaafar, J.; Ismail, A.F. Structure Formation in Anode and Its Effect on the Performance of Micro-Tubular SOFC: A Brief Review Graphical Abstract Keywords. *J. Membr. Sci. Res.* **2019**, *5*, 197–204. [CrossRef]
21. Zhou, J.; Liu, Q.; Zhang, L.; Pan, Z.; Chan, S.H. Influence of Pore Former on Electrochemical Performance of Fuel-Electrode Supported SOFCs Manufactured by Aqueous-Based Tape-Casting. *Energy* **2016**, *115*, 149–154. [CrossRef]
22. Weber, S.; Juckel, M.; Liu, Y.; Wieler, M.; Schneider, D.; Nestler, B.; Menzler, N.H.; Schmidt, V. Comparing the 3D Morphology of Solid-Oxide Fuel Cell Anodes for Different Manufacturing Processes, Annealing Times, and Operating Temperatures. *J. Electrochem. Soc.* **2025**, *172*, 044506. [CrossRef]
23. Mohanty, D.; Hung, J.; Chen, Y.; Hung, I.; Lin, Y. Optimization and Characterization of Porous Ni/YSZ Anode Microstructure for Solid Oxide Fuel Cell. *Ceram. Int.* **2025**, *51*, 22841–22848. [CrossRef]
24. Gomez-villalba, L.S.; Feijoo, J.; Eugenia, M.; Fort, R. In-Situ Electrochemical Synthesis of Inorganic Compounds for Materials Conservation: Assessment of Their Effects on the Porous Structure. *Ceram. Int.* **2021**, *47*, 30406–30424. [CrossRef]
25. Varanasi, S.; Gar, U.; Simon, G.P.; Garnier, G.; Batchelor, W. Novel In-Situ Precipitation Process to Engineer Low Permeability Porous Composite. *Sci. Rep.* **2018**, *8*, 10747. [CrossRef]
26. Hedayat, N.; Du, Y.; Ilkhani, H. Pyrolyzable Pore-Formers for the Porous-Electrode Formation in Solid Oxide Fuel Cells: A Review. *Ceram. Int.* **2018**, *44*, 4561–4576. [CrossRef]
27. Cigdem, T.; Onbilgin, S.; Timurkutluk, B.; Pamuk, I. Effects of Pore Former Type on Mechanical and Electrochemical Performance of Anode Support Microtubes in Solid Oxide Fuel Cells. *Int. J. Hydrogen Energy* **2022**, *47*, 11633–11643. [CrossRef]
28. Ahmad, S.H.; Jamil, S.M.; Othman, M.H.D.; Rahman, M.A.; Jaafar, J.; Ismail, A.F. Pore Former Addition in the Preparation of Highly Porous Anode Using Phase-Inversion Technique for Solid Oxide Fuel Cell. *J. Membr. Sci. Res.* **2019**, *5*, 268–273. [CrossRef]
29. Pavzderin, N.B.; Nikonov, A.V.; Paranin, S.N.; Kuterbekov, K.A.; Bekmyrza, K.Z. Pore-Forming Agents for the Supporting Ni-Based SOFC Anode. *Russ. J. Electrochem.* **2018**, *54*, 500–505. [CrossRef]
30. Choolaei, M.; Vostakola, M.F.; Horri, B.A. Recent Advances and Challenges in Thin-Film Fabrication Techniques for Low-Temperature Solid Oxide Fuel Cells. *Crystals* **2023**, *13*, 1008. [CrossRef]
31. Ma, G.; Xia, L.; Zhang, T.; Zhong, B.; Yang, H.; Xiong, L.; Huang, L.; Huang, X.; Wen, G. Permeability and Thermal Expansion Properties of Porous LAS Ceramic Prepared by Gel-Casting Method. *J. Eur. Ceram. Soc.* **2020**, *40*, 3462–3468. [CrossRef]
32. Hu, J.; Lü, Z.; Chen, K.; Huang, X.; Ai, N.; Du, X.; Fu, C.; Wang, J.; Su, W. Effect of Composite Pore-Former on the Fabrication and Performance of Anode-Supported Membranes for SOFCs. *J. Memb. Sci.* **2008**, *318*, 445–451. [CrossRef]

33. Nie, L.; Liu, J.; Zhang, Y.; Liu, M. Effects of Pore Formers on Microstructure and Performance of Cathode Membranes for Solid Oxide Fuel Cells. *J. Power Sources* **2011**, *196*, 9975–9979. [CrossRef]
34. Zhou, X.; Wang, J.; Zhang, J.; Pang, X.; Guo, X.; Sunarso, J.; Li, C.; Yu, F.; Yang, N.; Kawi, S. 3D Printing of Porous Zirconia Support for Solid Oxide Fuel Cells with High Cell Performance. *Ceram. Int.* **2024**, *50*, 28826–28836. [CrossRef]
35. Drozdz, E.; Stachura, M.; Wyrwa, J.; Rękas, M. Effect of the Addition of Pore Former: Graphite and Ammonium Bicarbonate on the Properties of Ni/Al2O3-3YSZ Composite Materials. *J. Therm. Anal. Calorim.* **2015**, *122*, 157–166. [CrossRef]
36. Turnbull, R.J.; Shearer, N.; Wilson, C. Cellulose Microfibrils as a Pore Former in Electroless Co-Deposited Anodes for Solid Oxide Fuel Cells. *ECS Meet. Abstr.* **2017**, *MA2017-03*, 356. [CrossRef]
37. Sarikaya, A.; Dogan, F. Effect of Various Pore Formers on the Microstructural Development of Tape-Cast Porous Ceramics. *Ceram. Int.* **2013**, *39*, 403–413. [CrossRef]
38. Lu, K.; Manjooran, N.J.; Murakami, R.; Pickrell, G. *Advances in Synthesis, Processing, and Applications of Nanostructures*; Wiley: Hoboken, NJ, USA, 2012; Volume 238, ISBN 9781118273272.
39. Ni, D.W.; Esposito, V.; Foghmoes, S.P.V.; Ramousse, S. Densification and Grain Growth Kinetics of $Ce_{0.9}Gd_{0.1}O_{1.95}$ in Tape Cast Layers: The Influence of Porosity. *J. Eur. Ceram. Soc.* **2014**, *34*, 2371–2379. [CrossRef]
40. Buvat, G.; Quarez, E.; Joubert, O. Influence of $La_2Mo_2O_9$ on the Sintering Behavior and Electrochemical Properties of Gadolinium-Doped Ceria. *Ceram. Int.* **2017**, *43*, 10137–10143. [CrossRef]
41. Lejček, P.; Schneeweiss, O. Solute Segregation at Ordered Grain Boundaries. *Surf. Sci.* **2001**, *487*, 210–222. [CrossRef]
42. Bi, L.; Fang, S.; Tao, Z.; Zhang, S.; Peng, R.; Liu, W. Influence of Anode Pore Forming Additives on the Densification of Supported $BaCe_{0.7}Ta_{0.1}Y_{0.2}O_{3-\delta}$ Electrolyte Membranes Based on a Solid State Reaction. *J. Eur. Ceram. Soc.* **2009**, *29*, 2567–2573. [CrossRef]
43. Fontaine, M.L.; Larring, Y.; Smith, J.B.; Raeder, H.; Andersen, Ø.S.; Einarsrud, M.; Wiik, K.; Bredesen, R. Shaping of Advanced Asymmetric Structures of Proton Conducting Ceramic Materials for SOFC and Membrane-Based Process Applications. *J. Eur. Ceram. Soc.* **2009**, *29*, 931–935. [CrossRef]
44. Lee, J.H.; Heo, J.W.; Lee, D.S.; Kim, J.; Kim, G.H.; Lee, H.W.; Song, H.S.; Moon, J.H. The Impact of Anode Microstructure on the Power Generating Characteristics of SOFC. *Solid State Ion.* **2003**, *158*, 225–232. [CrossRef]
45. Fu, C.; Ge, X.; Chan, S.H.; Liu, Q. Fabrication and Characterization of Anode-Supported Low-Temperature SOFC Based on Gd-Doped Ceria Electrolyte. *Fuel Cells* **2012**, *12*, 450–456. [CrossRef]
46. Lee, D.S.; Lee, J.H.; Kim, J.; Lee, H.W.; Song, H.S. Tuning of the Microstructure and Electrical Properties of SOFC Anode via Compaction Pressure Control during Forming. *Solid State Ion.* **2004**, *166*, 13–17. [CrossRef]
47. Sharif, S.M.; Golestani Fard, F.; Khatibi, E.; Sarpoolaky, H. Dispersion and Stability of Carbon Black Nanoparticles, Studied by Ultraviolet-Visible Spectroscopy. *J. Taiwan Inst. Chem. Eng.* **2009**, *40*, 524–527. [CrossRef]
48. Lowell, S.; Shields, J.E.; Thomas, M.A.; Thommes, M. *Characterization of Porous Solids and Powders: Surface Area, Pore Size, and Density*; Springer: Dordrecht, The Netherlands, 2004; ISBN 978-1-4020-2302-6.
49. Wang, Z.; Sun, K.; Shen, S.; Zhou, X.; Qiao, J.; Zhang, N. Effect of Co-Sintering Temperature on the Performance of SOFC with YSZ Electrolyte Thin Films Fabricated by Dip-Coating Method. *J. Solid State Electrochem.* **2010**, *14*, 637–642. [CrossRef]
50. Kim, M.; Lee, J.; Han, J.H. Fabrication of Anode Support for Solid Oxide Fuel Cell Using Zirconium Hydroxide as a Pore Former. *J. Power Sources* **2011**, *196*, 2475–2482. [CrossRef]

Disclaimer/Publisher's Note: The statements, opinions and data contained in all publications are solely those of the individual author(s) and contributor(s) and not of MDPI and/or the editor(s). MDPI and/or the editor(s) disclaim responsibility for any injury to people or property resulting from any ideas, methods, instructions or products referred to in the content.